Research Article

Pragati A. Shinde, Vaibhav C. Lokhande, Amar M. Patil, Taeksoo Ji, and Chandrakant D. Lokhande*

Design and synthesis of hierarchical mesoporous WO_3-MnO_2 composite nanostructures on carbon cloth for high-performance supercapacitors

https://doi.org/10.1515/eetech-2017-0005
Received May 11, 2017; accepted Aug 24, 2017

Abstract: To enhance the energy density and power performance of supercapacitors, the rational design and synthesis of active electrode materials with hierarchical mesoporous structure is highly desired. In the present work, fabrication of high-performance hierarchical mesoporous WO_3-MnO_2 composite nanostructures on carbon cloth substrate via a facile hydrothermal method is reported. By varying the content of MnO_2 in the composite, different WO_3-MnO_2 composite thin films are obtained. The formation of composite is confirmed by X-ray diffraction (XRD) and X-ray photoelectron spectroscopy (XPS) analyses. The Brunauer-Emmett-Teller (BET) analysis reveals maximum specific surface area of 153 m^2 g^{-1}. The optimized WO_3-MnO_2 composite electrode demonstrates remarkable electrochemical performance with high specific capacitance of 657 F g^{-1} at a scan rate of 5 mV s^{-1} and superior long-term cycling stability (92% capacity retention over 2000 CV cycles). Furthermore, symmetric flexible solid-state supercapacitor based on WO_3-MnO_2 electrodes has been fabricated. The device exhibits good electrochemical performance with maximum specific capacitance of 78 F g^{-1} at a scan rate of 5 mV s^{-1} and specific energy of 10.8 Wh kg^{-1} at a specific power of 0.65 kW kg^{-1}. The improved electrochemical performance could be ascribed to the unique combination of multivalence WO_3 and MnO_2 nanostructures and synergistic effect between them

Keywords: Composite, Mixed metal oxides, Supercapacitors, Specific energy, Thin film

***Corresponding Author: Chandrakant D. Lokhande:** Centre for Interdisciplinary Research, D. Y. Patil University, Kolhapur 416 006 (M.S.), India; Email: l_chandrakant@yahoo.com
Pragati A. Shinde, Amar M. Patil: Centre for Interdisciplinary Research, D. Y. Patil University, Kolhapur 416 006 (M.S.), India
Vaibhav C. Lokhande, Taeksoo Ji: Department of Electronics and Computer Engineering, Chonnam National University, 300 Yongbong-Dong, Puk-Gu, Gwangju 500-757, South Korea

1 Introduction

Supercapacitors are the most promising electrical energy storage devices which gained significant attention because of their desirable features like fast charging-discharging rates, high efficiency, long-term cycling stability and ease of operation [1–3]. Recently, the development of supercapacitors with superior cycling stability and high energy density without sacrificing its power density is highly recommended [4, 5]. Generally, transition metal oxides are widely used electrodes for the development of efficient supercapacitors [6, 7]. However, their poor electrical conductivity and limited cycle life restrict their further practical application. The composite supercapacitors are one of the impeding class of electrochemical capacitors with the prospect to deliver high energy density at high charging-discharging rates. Moreover, many research groups have prepared carbon based metal oxide composites to enhance the poor electrical conductivity of metal oxides. For example, MnO_2/CNT composite prepared by Li *et al.* [8] exhibited a specific capacitance of 201 F g^{-1}. Wang *et al.* [9] prepared MnO_2/carbon nanowires composite which exhibited a specific capacitance of 465 F g^{-1}. However, the use of carbon materials as a supercapacitor electrode decreases the cost-effectiveness of electrode and specific capacitance. Therefore, the extensive research efforts towards making efficient supercapacitor electrodes with low-cost and high performance remain a challenge. Meanwhile, highly conductive metal oxides are utilized for enhancing conductivity and electrochemical performance of metal oxide based supercapacitors [10–12].

The mixed metal oxide composites are widely used to enhance the electrochemical performance of metal oxides by expanding their redox activity, specific surface area as well as conductivity. The mixed metal oxides because of their different valencies provide additional redox sites during electrochemical reactions and thereby enhance the specific capacitance and energy density [13, 14]. Recently, various mixed metal oxide composite electrodes

such as NiO/Co_3O_4, Mn_3O_4/ Co_3O_4, $NiCo_2O_4/NiWO_4$ etc. have been regarded as best electrodes for next-generation supercapacitors [14–16].

Many research groups have reported WO_3 as an active electrode material for supercapacitors due to their excellent physico-chemical properties and diverse potential applications [17–19]. In previous studies, Kang *et al.* [20] prepared ordered mesoporous WO_3 with high electrical conductivity of 1.76 S cm^{-1} which is comparable to the conductivity of ordered mesoporous carbon (3.0 S cm^{-1}). Moreover, supercapacitors based on composite electrodes using MnO_2 are of significant importance because of their notable theoretical capacitance, abundant natural resources, low cost and environmental compatibility [21]. However, the intrinsically poor electrical conductivity of MnO_2 (10^{-5} to 10^{-6} S cm^{-1}) restricts its power performance. The individual capacitive performance of WO_3 and MnO_2 has been widely studied, however, there are only few reports on their composites. Therefore, in the present investigation, a simple synthesis strategy is employed to prepare WO_3-MnO_2 composite thin films on carbon cloth substrate. This approach has number of advantages such as, MnO_2 nanoparticles in the composite allow fast and reversible faradic reactions and reduces the ion diffusion length. WO_3 nanostructures with high conductivity provides a direct pathway for electron transport and create mesoporous channels for the effective transport of electrolyte ions. The main advantage of this composite electrode is that the composite electrode is capable of achieving superior cycling stability as compared to MnO_2 and higher storage capacity than the bare WO_3 electrode.

Herein, the synthesis of hierarchical mesoporous WO_3-MnO_2 composite nanostructures on carbon cloth using hydrothermal method is reported. By varying the content of MnO_2, different WO_3-MnO_2 composite films are obtained. The electrochemical performance of electrodes is investigated in a standard three-electrode cell with 1 M Na_2SO_4 solution as an electrolyte. The fabrication of mixed metal oxide composites on carbon cloth can provide a novel idea for the development of promising electrodes for supercapacitors.

2 Experimental

2.1 Synthesis of WO_3-MnO_2 composite thin films

The hydrothermal method is well suited for the preparation of composite materials. The WO_3-MnO_2 composite thin films were deposited directly on carbon cloth substrate by binder- and additive-free approach. Briefly, 0.1 M $Na_2WO_4{\cdot}2H_2O$ was dissolved in 75 ml of double distilled water (DDW). The resulting solution was sonicated for about 10 min. Further, 0.05 M $KMnO_4$ (75 ml) solution was added dropwise into above solution under continuous magnetic stirring at room temperature. Subsequently, the pH of resulting solution was maintained at ~2.0 by dropwise addition of 3 M HCl solution under stirring to form a suspension. Afterwards, the reaction mixture was placed in a teflon-lined stainless steel autoclave with a capacity of 200 ml. The well cleaned carbon cloth substrate (2×5 cm^2) was placed into the autoclave and maintained at 453 K for 12 h in an oven. The autoclave was naturally cooled down to room temperature and the carbon cloth coated with grey-brown material was taken out, washed repeatedly with DDW to remove residual nanoparticles and dried overnight. Furthermore, different WO_3-MnO_2composite thin films were obtained by varying the amount of $KMnO_4$ as 0.05, 0.075, 0.1 and 0.125 M while keeping other parameters the same. The films obtained with WO_3:MnO_2 molar ratios 1:0.5, 1:0.75, 1:1 and 1:1.25 are labelled as A:WMn, B:WMn, C:WMn and D:WMn, respectively. Schematic illustration for hydrothermal synthesis of WO_3-MnO_2 composite thin film is shown in Figure 1.

2.2 Characterization techniques

The WO_3-MnO_2 composite thin films were characterized by different physicochemical techniques. The surface morphologies of prepared thin films were monitored by field-emission scanning electron microscope (FE-SEM; JEOL JSM-6390). The energy dispersive X-ray analysis (EDAX) was employed for the chemical characterization or elemental analysis of the sample. The X-ray diffraction study was performed using Bruker AXS D8 advance model with copper radiation (λ = 1.5418 Å). The X-ray photoelectron spectrum (XPS) was analysed using ESCALAB 250Xi X-ray photoelectron spectrometer microprobe. The N_2 adsorption-desorption isotherms were measured on a Quantachrome, Model-NOVA 1000E. All electrochemical characterizations were carried on a automatic battery cycler (WBCS3000) using the standard three electrode system with 1 M Na_2SO_4 as an electrolyte, prepared thin films as a working electrodes, platinum foil as a counter electrode and saturated calomel electrode (SCE) as a reference electrode. Electrochemical impedance spectroscopy (EIS) measurement was performed using electrochemical workstation (ZIVE SP 5).

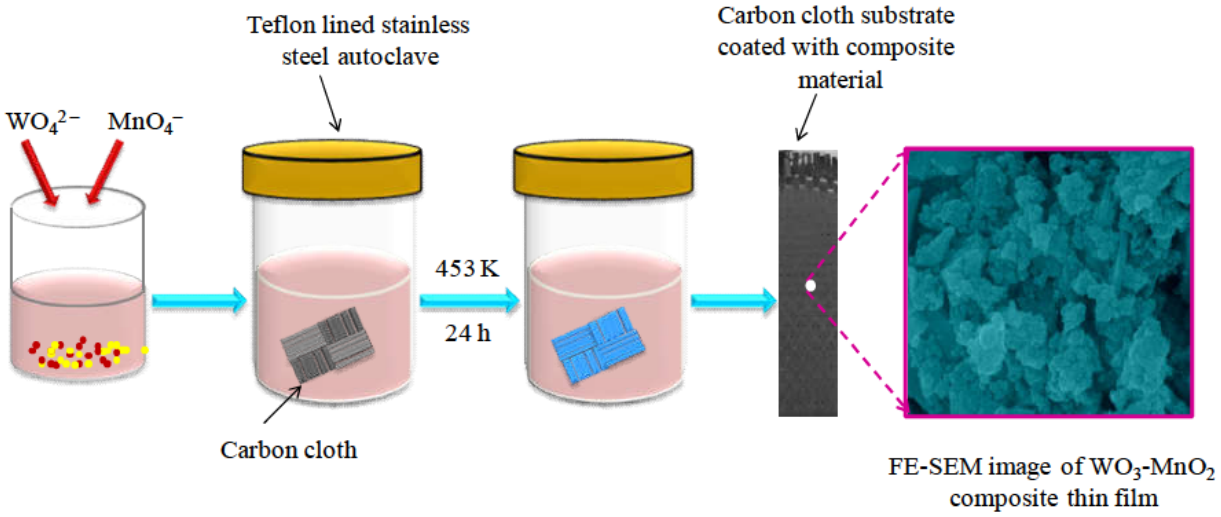

Figure 1: Schematic illustration for hydrothermal synthesis of WO_3-MnO_2 composite thin film.

3 Results and discussion

3.1 Surface morphological and elemental studies

The FE-SEM images of WO_3-MnO_2 composite thin films prepared with various precursor's molar ratio at two different magnifications of 13,000 X and 80,000 X are shown in Figure 2. The composite thin films demonstrate porous structure with agglomerated surface morphology, which is composed of bunches of nanostructures with WO_3 3-dimensional (3-D) cubes and MnO_2 nanoparticles. The 3-D cubes and nanoparticles together form large number of mesopores in the composite material.

The surface morphology of A:WMn (1:0.5) thin film demonstrates that the film surface is covered with rough and irregularly shaped grains in the form of cubes (Figure 2(a-b)). The growth of MnO_2 nanoparticles into clusters is clearly observed on these cubes. The 3-D cubes have diameters in the range of 400-500 nm. The surface of B:WMn (1:0.75) thin film in Figure 2(c-d) depicts that the diameter of 3-D cubes is reduced to half with increasing concentration of Mn in composite. The increased number of MnO_2 nanoparticles covers the surface of 3-D cubes. The 3-D cubes have diameters in the range of 200-300 nm. With further increase in concentration of Mn for C:WMn (1:1) thin film, the 3-D cube structure of WO_3 collapses and forms small nanoparticles as shown in Figure 2(e-f)). The small nanoparticles agglomerated together to form a cluster of nanoparticles. The cluster of nanoparticles with irregular shape and size are randomly oriented all over the carbon cloth substrate. This causes the formation of numerous mesopores on the surface and in the bulk of active material. The intermediate space between these clusters provides an easy path for the diffusion and transportation of electrolyte ions and decreases the ion diffusion length. Such a nanostructured mesoporous surface morphology provides numerous electrochemically active sites during charge intercalation/deintercalation process and improves the rate of electrochemical reactions. The porosity of film enhances the interaction between active material and the electrolyte which thus improves the electrochemical performance. Impressively, MnO_2 nanoparticles possess high specific surface area to store the charge and WO_3 nanoparticles enhance the rate of penetration of electrolyte into the interior of porous nanostructure. Moreover, addition of extra Mn in D:WMn (1:1.25) thin film shows the formation of slightly compact surface morphology (Figure 2(g-h)). At higher concentration of Mn, number of nanoparticles in composite thin film are increased. These nanoparticles are attached to the cluster of nanoparticles. As a result, clusters of nanoparticles grow into a larger size and form a compact surface of film. The compact surface of D:WMn thin film reduces the porosity and active surface area during electrochemical reactions as compared to C:WMn thin film.

The molar ratio of precursors ($Na_2WO_4 \cdot 2H_2O/KMnO_4$) is one of the important parameters to obtain the required WO_3-MnO_2 composite thin films. For C:WMn thin film equimolar concentration of both precursors form highly porous surface morphology. The porous surface provides large numbers of electrochemically active sites on the electrode during electrochemical reaction. Also, the synthesis of WO_3-MnO_2 composite directly on conducting substrate enhances the electrochemical performance of supercapac-

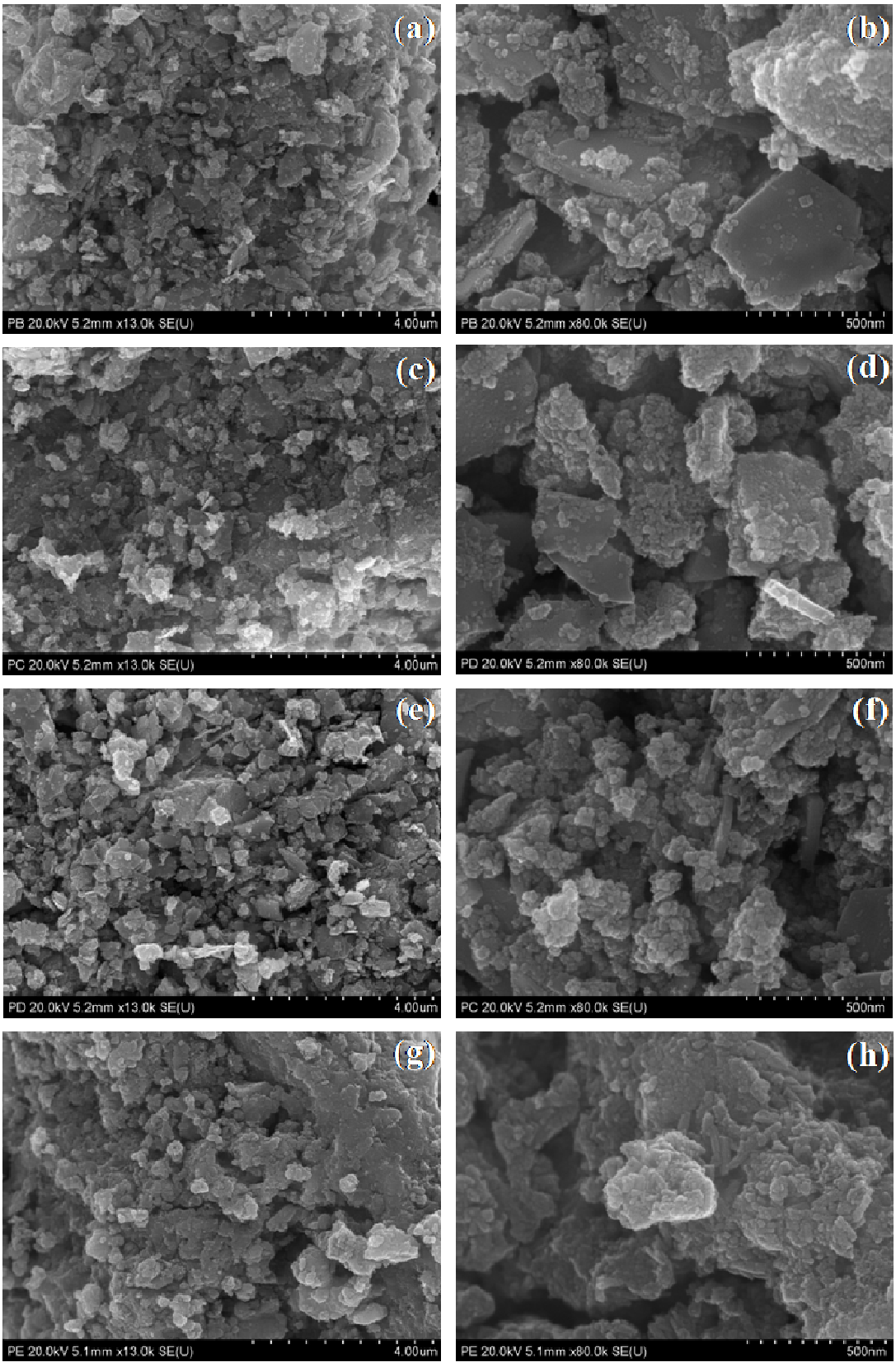

Figure 2: The FE-SEM images of (a-b) A:WMn, (c-d) B:WMn, (e-f) C:WMn, and (g-h) D:WMn thin films at magnifications of 13,000 X and 80,000 X.

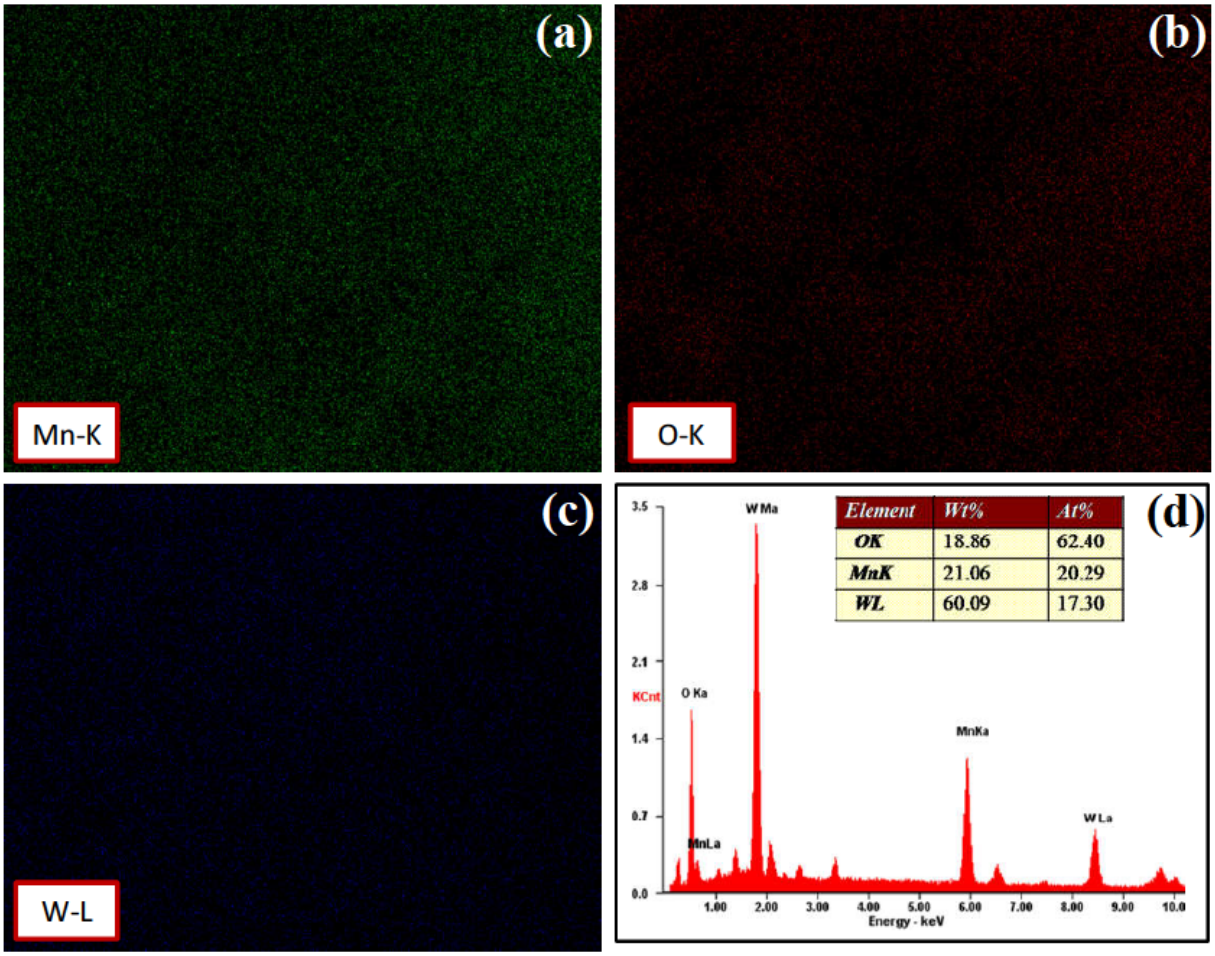

Figure 3: The EDAX elemental mapping of C:WMn thin film a) Mn-K (green), b) O-K (red), c) W-L (blue) and d) the energy-dispersive X-ray pattern of C:WMn thin film, inset chart show atomic percentage of O, Mn and W.

itor electrode. The direct growth of nanostructured materials on conducting surface finds its own contact with the current collector. Therefore, each nanostructured material is participating in electrochemical reactions more effectively [22].

The EDAX elemental mapping analysis is used to observe the elemental composition and spatial distribution of elements present in the composite material. Figure 3(a-c) illustrates the elemental mapping of C:WMn thin film. The EDAX elemental mapping shows that, Mn (green), O (red) and W (blue), elements are detected clearly. These elements are homogeneously distributed over the entire matrix of C:WMn thin film. The EDAX analysis spectrum and atomic percentage in the C:WMn thin film is presented in Figure 3(d). The peaks of W, Mn and O are clearly observed in the EDAX spectrum. These results visualize that WO_3 and MnO_2 nanostructures in the composite are in physical contact with each other and assist in making good electrical contact with the support substrate.

3.2 Structural studies

The crystal structure of WO_3-MnO_2 composite thin films is examined by XRD analysis. Figure 4 shows the XRD patterns of A:WMn, B:WMn, C:WMn and D:WMn thin films. The XRD patterns of all the films represent the same peaks. All the diffraction peaks are well indexed to the hexagonal phase of WO_3 (JCPDS 33-1387) and orthorhombic phase of MnO_2 (JCPDS 42-1316). The sharp and intense peaks indicate good crystallinity of WO_3-MnO_2 thin films. The results confirm that WO_3-MnO_2 composites are successfully synthesized. Further, to confirm the chemical constituents and oxidation states, XPS analysis of C:WMn thin film is performed. The survey scan spectrum in Figure 5(a) reveals that the surface of C:WMn thin film is composed of W, Mn, O and C elements. Further, Figure 5(b) illustrates the XPS spectrum of W 4f core level. The peaks situated at binding energies of 38.04 and 35.92 eV correspond to W $4f_{5/2}$ and W $4f_{7/2}$ levels, respectively, with a spin-orbit

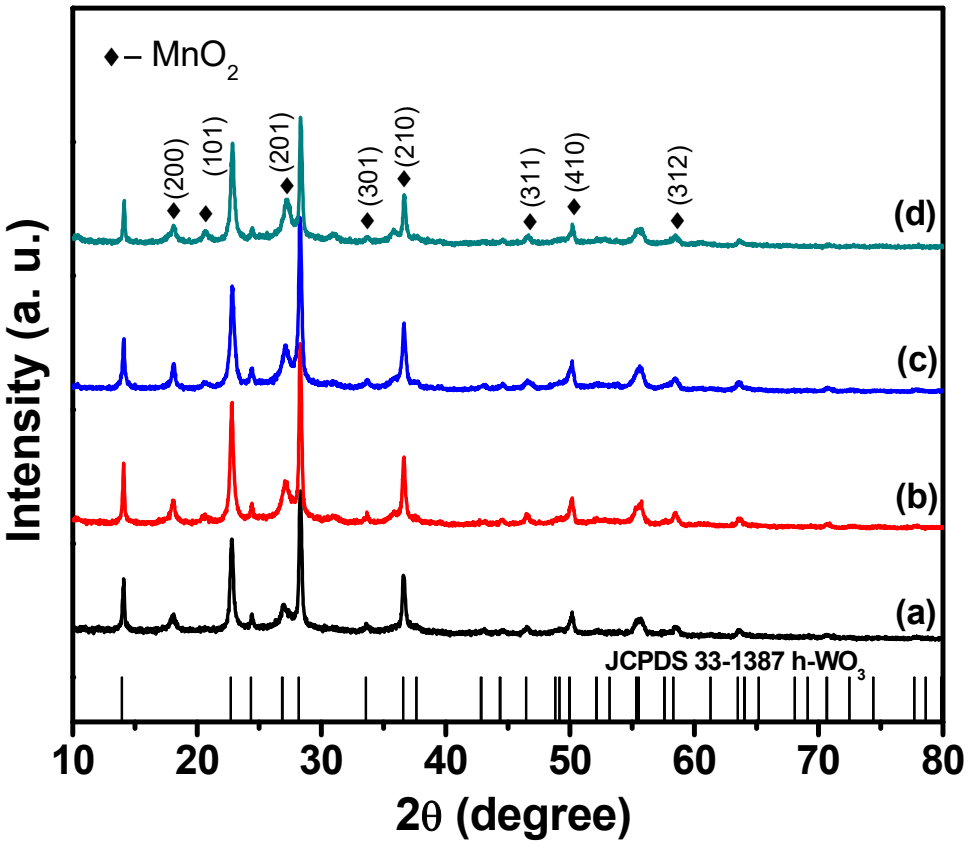

Figure 4: The XRD patterns of a)A:WMn, b)B:WMn, c)C:WMn and d)D:WMn.

splitting of 2.12 eV. These peaks correspond to 6^+ oxidation state of W [23]. The Mn 2p core level spectrum reveals two major peaks at binding energies of 654.3 and 642.6 eV related to Mn $2p_{1/2}$ and Mn $2p_{3/2}$ levels, respectively (Figure 5(c)). The spin-orbit separation of 11.7 eV is in good agreement with previous reports for MnO_2 [24, 25]. In addition to this, the fitted O 1s spectrum is characterized by three peaks as shown in Figure 5(d). The two peaks at 532.86 and 531.96 eV are attributed to the adsorption of oxygen and water molecules on WO_3-MnO_2 composite surface, and a peak at 530.5 eV corresponds to the O^{2-} band with W and Mn. These results also confirm the formation of WO_3-MnO_2 composite, which is in good agreement with the earlier XRD analysis.

3.3 Electrochemical studies

The cyclic voltammetry (CV) curves of A:WMn, B:WMn, C:WMn and D:WMn thin films measured in 1 M Na_2SO_4 electrolyte at a scan rate of 100 mV s^{-1} in a potential range of −0.6 to +0.6 V/SCE are shown in Figure 6(a). As shown in figure, C:WMn thin film exhibits larger area under the CV curve as compared to A:WMn, B:WMn and D:WMn thin films, which means that it gives higher specific capacitance. The result obtained here agrees with the FE-SEM morphologies, signifying that nanoparticles composed into a porous surface of C:WMn thin film provides good surface area and improves charge diffusion/transportation into the interior region. Furthermore, CV curves of C:WMn thin film at different scan rates (5 - 100 mV s^{-1}) are shown in Figure 6(b). As scan rate increases area under the CV curve also increases. The CV curves for all samples exhibit direct proportion between currents and scan rate of voltammograms, this indicates perfectly capacitive features. The CV curves demonstrate symmetric rectangular shape with no noticeable redox peaks. The absence of redox peaks is attributed to the fast and reversible redox reactions in between active electrode and electrolyte at steady rate [26, 27].

The specific capacitance from CV curve is calculated using following formula;

$$C_s = \frac{1}{mv(V_{\max} - V_{\min})} \int_{V_{\min}}^{V_{\max}} I(V)dv \qquad (1)$$

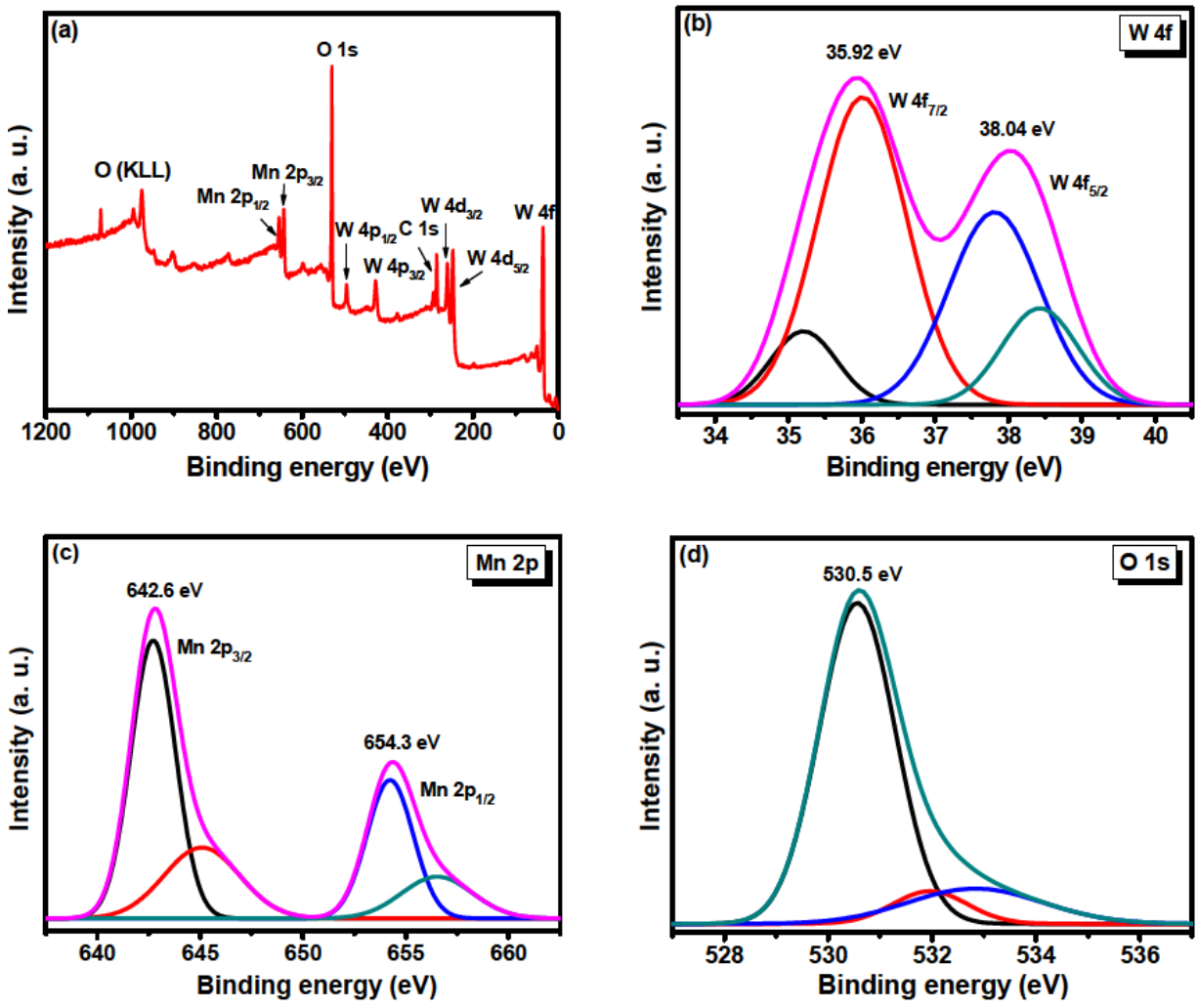

Figure 5: The XPS spectra of C:WMn thin film a) survey scan, b) W 4f core level, c) Mn 2p core level, and d) O 1s core level.

where, C_s is the specific capacitance, m is the mass of deposited material, $V_{max} - V_{\min}$ is the potential window, I is the average current for unit area dipped in the electrolyte. The variation of C_s with scan rate is illustrated in Figure 6(c). The maximum C_s of 657 F g^{-1} is obtained at scan rate of 5 mV s^{-1}. The maximum value of C_s for C:WMn thin film is due to its highly porous and fine nanoparticles composed surface morphology, which in turn offers a large number of active sites and intermediate space for charge transfer and storage. Also, the different valencies of W and Mn in the composite allow multiple electrochemical reactions, which thus enhance the C_s and energy storage capacity of the electrode. The obtained value of specific capacitance is larger than the earlier reports. For instance, Yuan *et al.* [28] obtained C_s of 363 F g^{-1} for electrodeposited nano-$WO_3 \cdot H_2O/MnO_2$ composite thin film.

To evaluate C_s and rate capability of C:WMn thin film, the charge-discharge measurements are performed. The galvanostatic charge-discharge (GCD) curves of A:WMn, B:WMn, C:WMn and D:WMn thin films at constant current density of 2 mA cm^{-2} are shown in Figure 6(d). The maximum discharge time is clearly observed for C:WMn thin film. This suggests that composition of W and Mn in C:WMn thin film makes good stoichiometric thin film, which helps to improve its electrochemical performance as compared to other films. Furthermore, Figure 6(e) displays the GCD curves of C:WMn thin film at different current densities (2 - 8 mA cm^{-2}). The non-linear behavior of charge-discharge curves confirms its pseudocapacitive feature. This behavior is due to the electrochemical adsorption-desorption reactions at the interface of electrode and electrolyte [29].

The C_s from GCD curve is calculated using following formula;

$$C_s = \frac{I_d \times T_d}{\Delta V \times m} \tag{2}$$

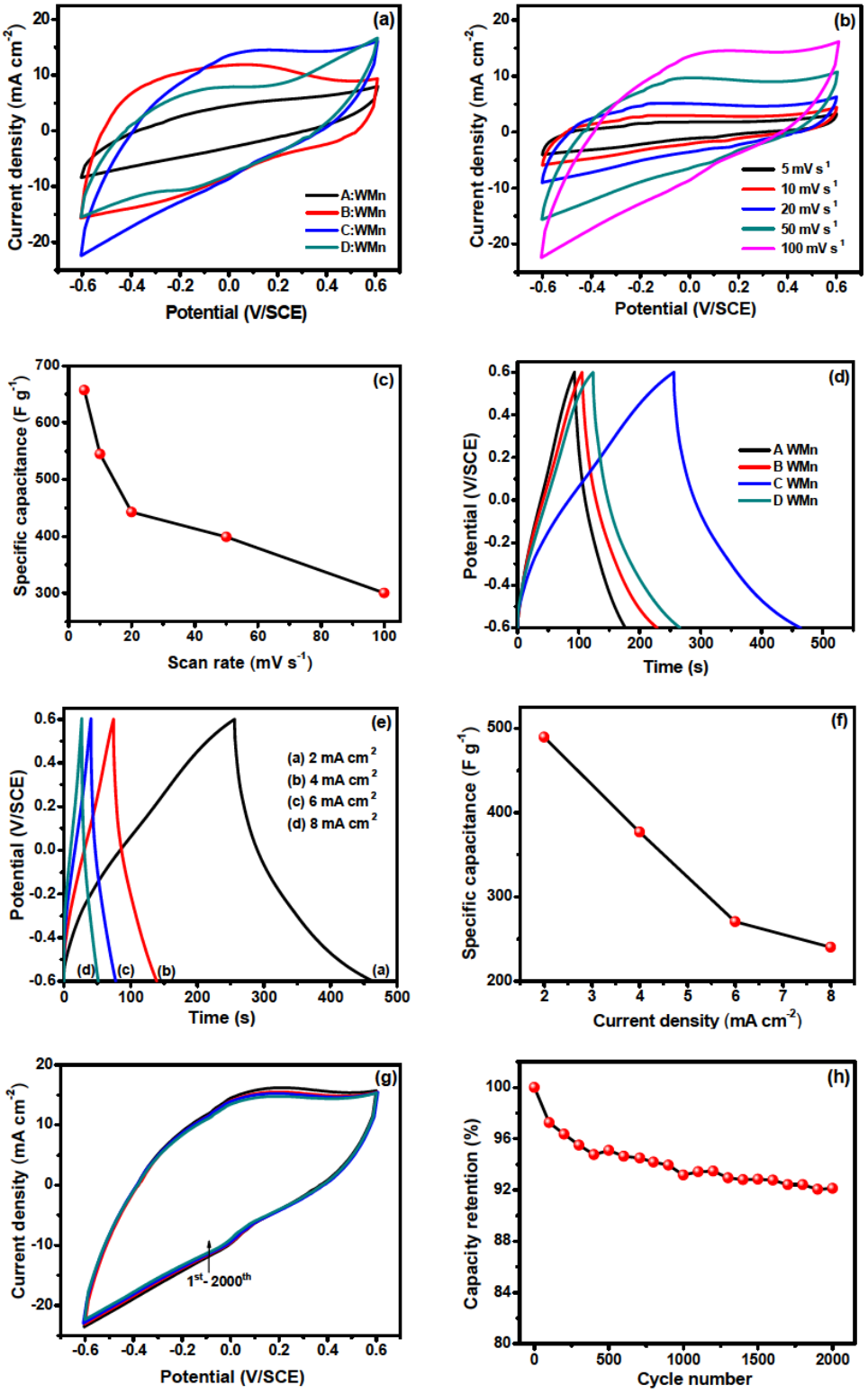

Figure 6: (a) The comparative CV curves of A:WMn, B:WMn, C:WMn and D:WMn thin films at a scan rate of 100 mV s^{-1}, (b) the CV curves of C:WMn thin film at different scan rates, (c) the plot of C_s versus scan rate, (d) the GCD curves of A:WMn, B:WMn, C:WMn and D:WMn thin films at a current density of 2 mA cm^{-2}, (e) the GCD curves of C:WMn thin film at different current densities, (f) the plot of C_s versus current density, (g) the CV curves for 1^{st}–2000^{th} cycles and (h) the plot of capacity retention versus cycle number for C:WMn thin film.

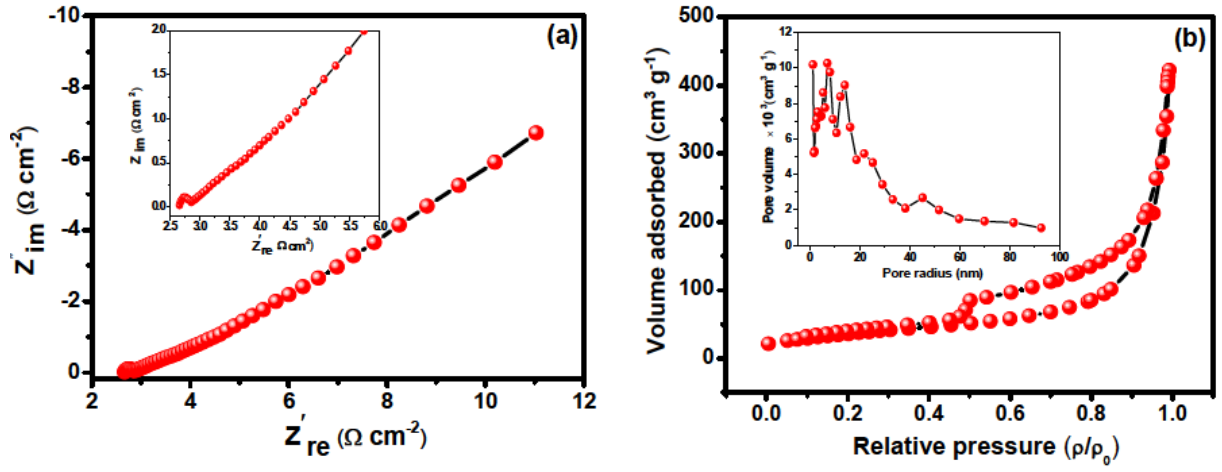

Figure 7: (a) The Nyquist plot (inset figure shows magnified Nyquist plot) and (b) the N_2 adsorption-desorption isotherms (inset figure shows pore size distribution curve) for C:WMn sample.

where, I_d is the discharge current, T_d is the discharge time and ΔV is the potential window. The estimated values of C_s with respect to current density are plotted in Figure 6(f). The C:WMn thin film demonstrates C_s of 492 F g^{-1} at current density of 2 mA cm^{-1} and it decreases for further higher current densities.

The long-term cycling stability of supercapacitor electrode is crucial for measuring capability of the electrode for many practical applications. Therefore, the cycling stability of C:WMn thin film is recorded in 1 M Na_2SO_4 electrolyte using CV measurement for 2000 cycles at a scan rate of 100 mV s^{-1} . Figure 6(g) illustrates CV curves of C:WMn thin film for 1^{st} – 2000^{th} cycles. The plot of variation of capacity retention with cycle number is demonstrated in Figure 6(h). The C:WMn thin film depicts 92% capacity retention after 2000 CV cycles. The uniform distribution of nanoparticles on carbon cloth surface makes good adhesion with the current collector and stabilizes the resulting nanostructure. As a result, the loss of active material in electrolyte during cycling is very less for C:WMn composite thin film, which gives higher stability.

Electrochemical impedance spectroscopy (EIS) study is employed to evaluate equivalent series resistance and charge transfer rate of electrolyte ions at the electrode/electrolyte interface. The Nyquist plot of C:WMn thin film in the frequency range of 10 mHz to 100 kHz is illustrated in Figure 7(a). The distinct region provided by Nyquist plot explains the charge transfer process at the electrode/electrolyte interface. The Nyquist plot consists of high-frequency semicircle arc and low-frequency straight line. The equivalent series resistance (R_s) obtain from the X-axis intercept of Nyquist plot is associated with the combination of bulk resistance of electrode, ionic resistance of electrolyte and contact resistance between active material and current collector [30]. The semicircle at high to medium frequency region corresponds to the charge transfer resistance (R_{ct}) and double layer capacitance. The low-frequency straight line, inclined at an angle of 45° to Z'-axis represents the diffusion process. The values of R_s and R_{ct} from Nyquist plot are 2.65 and 0.25 Ω cm^{-2}, respectively. The smaller value of R_s and R_{ct} signifies the improved conductivity and charge storage capacity of C:WMn thin film.

As C:WMn thin film shows superior electrochemical performance as compared to other thin films, therefore, the texture properties of C:WMn composite were studied by Brunauer-Emmett-Teller (BET) and N_2 adsorption-desorption isotherms as illustrated in Figure 7(b). The C:WMn composite shows a typical type III isotherm with hysteresis loop in a high relative pressure (P/P_0) range of 0.5–1.0. The pore size distribution in C:WMn composite is analyzed using Barrett-Joyner-Halenda (BJH) technique. The inset of Figure 7(b) illustrates the BJH pore size distribution plot for C:WMn sample. It is seen that, C:WMn composite revealed characteristics of mesoporous structure with average mesopores in the radius of ~1-18 nm. The C:WMn composite exhibits BET surface area of 153 m^2 g^{-1}. The high BET surface area and mesoporous structure improve the electron and ion transport, which result in the high electrochemical capacity of WO_3-MnO_2 composite. The obtained specific surface area for WO_3-MnO_2 composite is relatively high. For instance, Gao *et al.* [31] obtained a specific surface area of 8.25 m^2 g^{-1} for hydrothermally prepared WO_3-SnO_2 composite.

The composition of composite thin film is very important for making high-performance mixed metal oxide

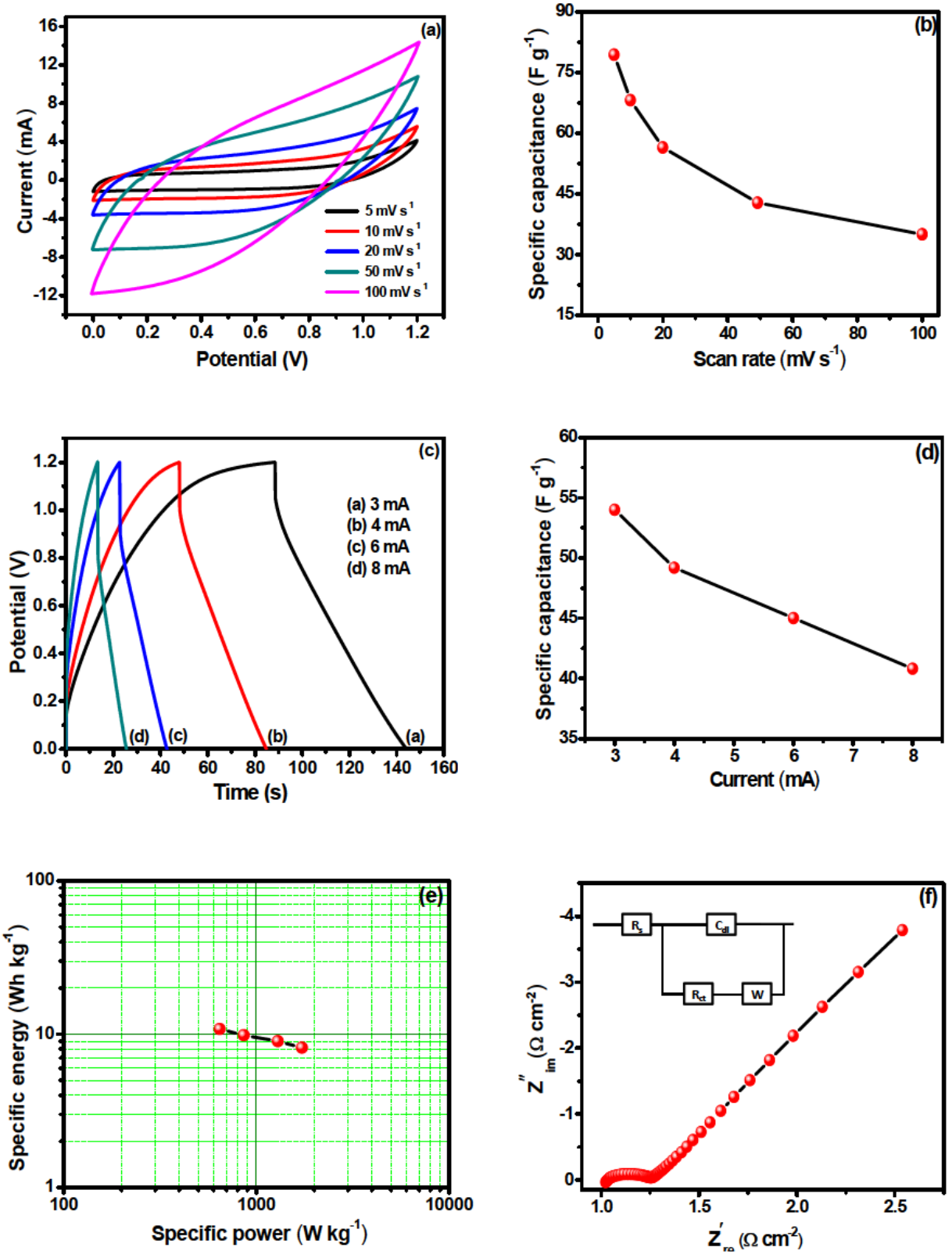

Figure 8: (a) The CV curves of C:WMn symmetric FSS-SCs device at different scan rates, (b) the plot of C_s versus scan rate, (c) the GCD curves of C:WMn symmetric FSS-SCs device at different currents, (d) the plot of C_s versus current, (e) the Ragone plot and (f) the Nyquist plot (inset figure shows equivalent circuit) of C:WMn symmetric FSS-SCs device.

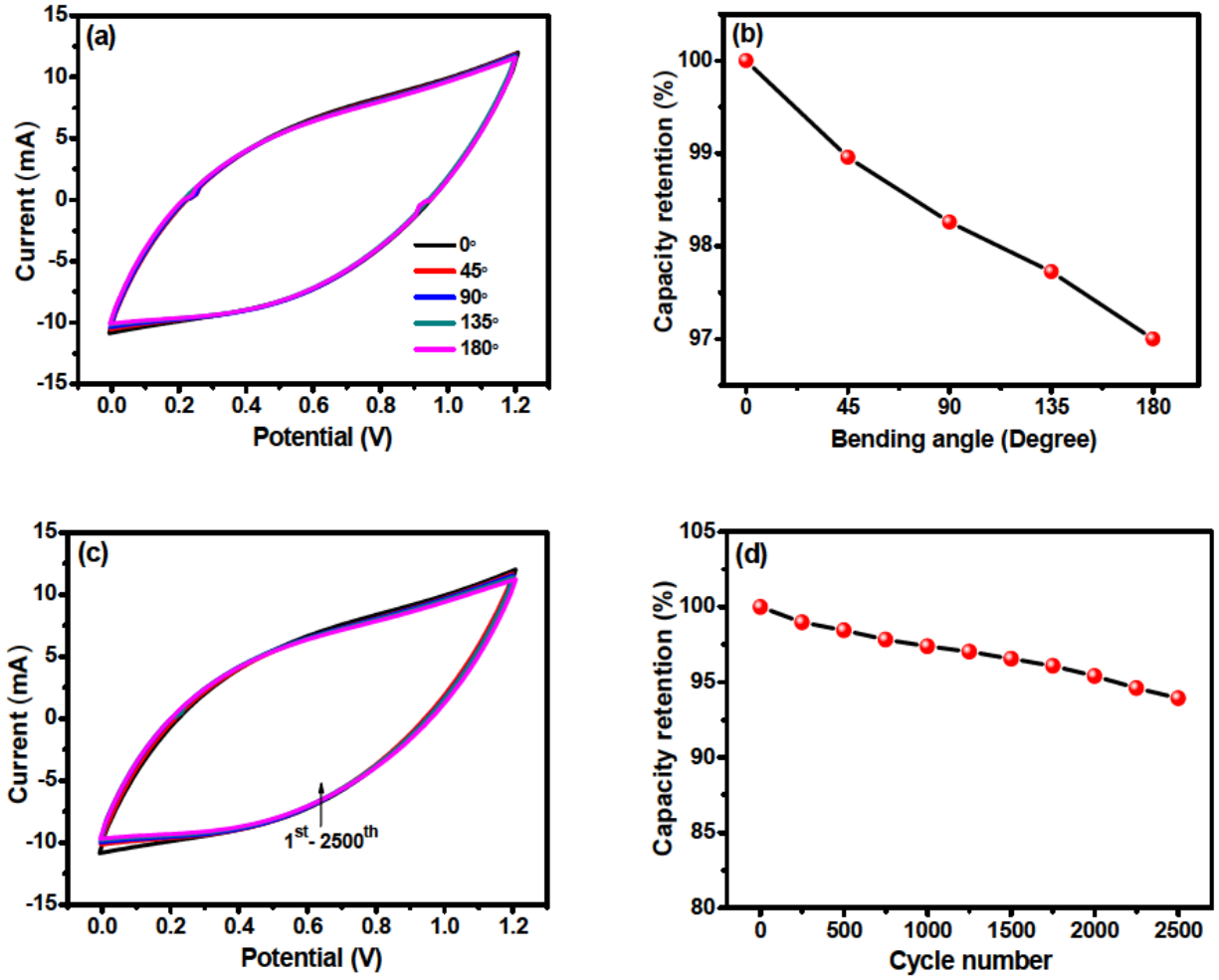

Figure 9: (a) The CV curves of C:WMn symmetric FSS-SCs device at different bending angles, (b) the variation of capacity retention at different bending angles, (c) the CV curves for 1^{st}–2500^{th} cycles and (d) the plot of capacity retention versus cycle number for C:WMn symmetric FSS-SCs device.

thin film. The nanoparticles composed porous structure of C:WMn thin film stabilizes the resulting nanostructure and improves its electrochemical performance. Also, the binder-free electrode enhances the electronic conductivity of supercapacitor. MnO_2 nanoparticles in the composite allow fast and reversible faradic reactions and reduce the ion diffusion length. WO_3 nanostructures with high conductivity provide direct pathway for electron transport. Moreover, the combination of MnO_2 and WO_3 with different redox transition states provides large number of electrochemically active sites for electrochemical redox reactions. The high specific surface area and mesoporous nanostructure of C:WMn thin film store more charges which leads to improved overall electrochemical performance.

3.4 Electrochemical properties of symmetric flexible solid-state supercapacitors (FSS-SCs) device

To further investigate practical applicability of C:WMn thin film for portable electronic appliances, C:WMn based symmetric FSS-SCs device is fabricated. For this, C:WMn thin films are prepared on 4.5×5 cm^2 area flexible carbon cloth substrates and utilized to fabricate FSS-SCs device. Carboxymethyl cellulose-sodium sulphate (CMC-Na_2SO_4) gel electrolyte was prepared for symmetric FSS-SCs device in order to correlate with the electrochemical performance of C:WMn electrode. The CMC-Na_2SO_4 gel acts as both separator as well as electrolyte. The solid-state gel electrolyte prevents the dissolution of active material into the electrolyte and hence increases the cycling stability of the device.

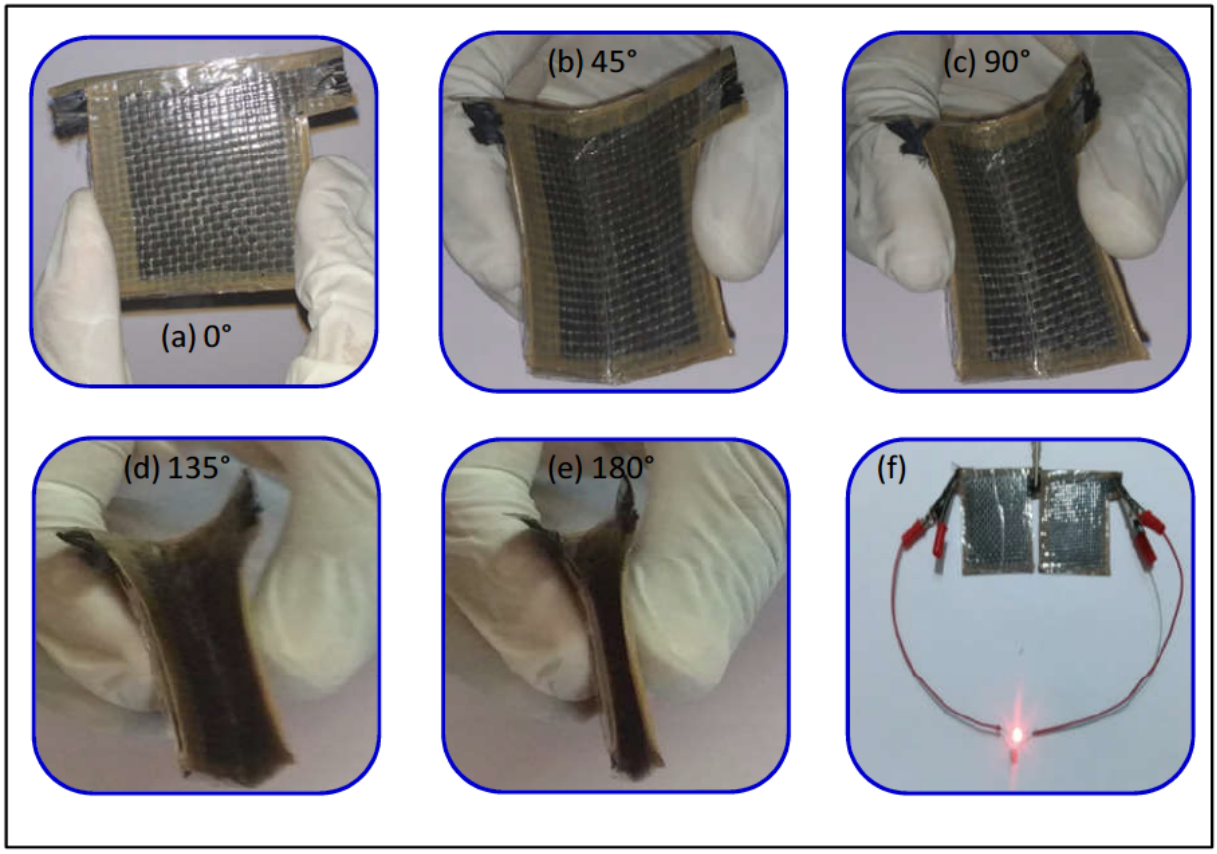

Figure 10: The digital photographs of (a-e) C:WMn symmetric FSS-SCs device at different bending angles and (f) the demonstration of two C:WMn symmetric FSS-SCs device in series combination by lighting red LEDs.

Figure 8(a) shows the CV curves of C:WMn symmetric FSS-SCs device at various scan rates (5 - 100 mV s^{-1}) within the potential window of 0 to +1.2 V. The CV curves illustrate symmetric nature along both cathodic and anodic directions, indicating better pseudocapacitive behaviour of the device. The area under the curve increases with increasing scan rate. The CV curves maintain their shape even at high scan rate of 100 mV s^{-1}, which indicates high rate capability of the device. The plot of C_s versus scan rate is demonstrated in Figure 8(b). It is observed that, C_s of C:WMn symmetric FSS-SCs device decreases with increasing scan rate, which could be due to the insufficient time for electrochemical reactions at the electrode. The device exhibits maximum C_s of 78 F g^{-1} at a scan rate of 5 mV s^{-1}. The GCD curves of C:WMn symmetric FSS-SCs device at different currents (3 - 8 mA) are presented in Figure 8(c). During charging-discharging process, small IR drop is observed, which indicates capacitive features and ultrafast charge-discharge rate of device. The increase in charging-discharging time with decrease in current is clearly seen. This is due to the limitations in charge-transport process at higher current density. The plot of C_s versus different currents is shown in Figure 8(d). The maximum C_s of 54 F g^{-1} is obtained at current of 3 mA and remained 41 F g^{-1} at higher current of 8 mA. Moreover, Ragone plot demonstrating the relationship between specific energy (SE) and specific power (SP) is employed in order to estimate the operational performance/efficiency of supercapacitor device.

The SE and SP are calculated from the discharge curve according to the following formulae;

$$SE = \frac{0.5 \times C_s \times ({V^2}_{\max} - {V^2}_{\min})}{3.6} \quad (3)$$

and

$$SP = \frac{ED \times 3600}{T_d} \quad (4)$$

The Ragone plot for C:WMn symmetric FSS-SCs device is presented in Figure 8(e). The C:WMn symmetric FSS-SCs device demonstrates maximum SE of 10.8 Wh kg^{-1} at SP of 0.65 kW kg^{-1}. Impressively, device demonstrates SP of 1.73 kW kg^{-1} maintaining SE of 8.16 Wh kg^{-1} at current of 8 mA. In addition to this, Nyquist plot of C:WMn symmetric FSS-SCs device within the frequency range of 10 mHz to 100 kHz is shown in Figure 8(f). The Nyquist plot consists of a small semicircle arc in the high-frequency region and

straight line in the low-frequency region. The equivalent circuit used for fitting impedance data is shown in inset of Figure 8(f). From impedance plot R_s and R_{ct} of C:WMn symmetric FSS-SCs device are about 1.7 and 1.17 Ω cm^{-2}, respectively. The smaller values of R_s and R_{ct} signify the mesoporous structure of active electrode which facilitates efficient accessibility of electrolyte ions at the interior of active material and smaller ion diffusion path.

The mechanical flexibility of FSS-SCs device is essential for its practical application. To investigate the mechanical flexibility of C:WMn symmetric FSS-SCs device, CV measurements are carried out at different bending angles (0-180°) at the fixed scan rate of 100 mV s^{-1} as shown in Figure 9(a). The shape of CV curves remains almost same even at bending angle of 180°. This indicates the better adhesion of active electrode material with the support substrate and good interface between active material and CMC-Na_2SO_4 gel electrolyte. The plot of capacity retention with different bending angles is shown in Figure 9(b). The C:WMn symmetric FSS-SCs device exhibits good mechanical flexibility with 96.8% capacity retention at bending angle of 180°. The better cycling stability of the device is primary requirement for its practical applications. Therefore, the stability of device is tested for 2500 CV cycles at a scan rate of 100 mV s^{-1}. Figure 9(c) shows CV curves of C:WMn symmetric FSS-SCs device for 1^{st}–2500^{th} cycles and Figure 9(d) depicts the plot of capacity retention versus cycle number for C:WMn symmetric FSS-SCs device. More strikingly, the device demonstrates capacity retention of 94% over 2500 CV cycles.

The digital photographs of C:WMn symmetric FSS-SCs device at different bending angles are shown in Figure 10(a-e). In order to demonstrate practical application of C:WMn symmetric FSS-SCs device, two C:WMn symmetric FSS-SCs devices are connected in series as shown in Figure 10(f). The device was charged to 2.5 V for 30 s and powered red light emitting diode (LED). These results show good performance of C:WMn symmetric FSS-SCs device and confirm that C:WMn thin film is promising electrode for practical applications.

4 Conclusions

The additive- and binder-free approach is employed for the direct synthesis of WO_3-MnO_2 composite thin films on carbon cloth using hydrothermal method. By varying the content of MnO_2 in the composite different stoichiometric WO_3-MnO_2 composite thin films are obtained. The C:WMn composite thin film with equimolar concentrations of both W and Mn precursors yield mesoporous structure with high specific surface area of 153 m^2 g^{-1}. Also, it demonstrates remarkable electrochemical performance with high specific capacitance of 657 F g^{-1} at a scan rate of 5 mV s^{-1} and good capacity retention (92% over 2000 CV cycles). The C:WMn symmetric FSS-SCs device exhibits specific capacitance of 78 F g^{-1} at a scan rate of 5 mV s^{-1} and specific energy of 10.8 Wh kg^{-1} at specific power of 0.65 kW kg^{-1} with good mechanical flexibility and stability. This synthesis method provides a new approach to increase the electrical conductivity and electrochemical performance of transition metal oxides for potential applications in supercapacitors and other energy storage devices.

Acknowledgement: Authors are grateful to Department of Science and Technology (DST) Govt. of India for providing financial support through major research project EMR/2016/001677 dated January 13, 2017.

References

[1] J. Luo, W. Zhong , Y. Zou, C. Xiong, W. Yang, J. Power Sources 319 (2016) 73.
[2] S. Chen, Wei. Xing, J. Duan, X. Hu, S. Z. Qiao, J. Mater. Chem. A 1 (2013) 2941.
[3] D. P. Dubal, N. R. Chodankar, Z. Caban-Huertas, F. Wolfart, M. Vidotti, R.Holze, C. D. Lokhande, P. Gomez-Romero, J. Power Sources 308 (2016) 158.
[4] P. A. Shinde, N. R. Chodankar, V. C. Lokhande, A. M. Patil, T. Ji, J. H. Kim, C. D. Lokhande, RSC Adv. 6 (2016) 113442.
[5] J. Liu, J. Jiang, M. Bosman, H. J. Fan, J. Mater. Chem. 22 (2012) 2419.
[6] X. W. Wang, D. L. Zheng, P. Z. Yang, X. E. Wang, Q. Q. Zhu, P. F. Ma, L. Y. Sun, Chem. Phys. Letters 667 (2017) 260.
[7] P. A. Shinde, V. C. Lokhande, N. R. Chodankar, T. Ji, J. H. Kim, C. D. Lokhande, J. Colloid Interface Sci. 483 (2016) 261.
[8] L. Li, Z. A. Hu, N. An, Y. Y. Yang, Z. M. Li, H. Y. Wu, J. Phys. Chem. C 118 (2014) 22865.
[9] B. Wang, J. Qiu, H. Feng, N. Wang, E. Sakai, T. Komiyam, Electrochim. Acta 212 (2016) 710.
[10] J. C. Chou, Y. L. Chen, M. H. Yang, Y. Z. Chen, C. C. Lai, H. T. Chiu, C. Y. Lee, Y. L. Chueh, J. Y. Gan, J. Mater. Chem. A 1 (2013) 8753.
[11] S. N. Pusawale, P. R. Deshmukh, J. L. Gunjakar, C. D. Lokhande, Mater. Chem. Phys. 139 (2013) 416.
[12] J. Cao, M. Safdar, Z. Wang, J. He, J. Mater. Chem. A 1 (2013) 10024.
[13] K. Wang, Z. Zhang, X. Shi, H. Wang, Y. Lu, X. Ma, RSC Adv. 5 (2015) 1943.
[14] H. Pang, J. Deng, J. Du, S. Li, J. Li, Y. Ma, J. Zhang, J. Chen, Dalton Trans. 41 (2012) 10175.
[15] U. M. Patil, S. B. Kulkarni, V. S. Jamadade, C. D. Lokhande, J. Alloys Compd. 509 (2011) 1677.
[16] C. C. Hu, C. W. Wang, T. H. Wu, K. H. Chang, Electrochim. Acta 85 (2012) 90.

[17] C. A. Bignozzi, S. Caramori, V. Cristino, R. Argazzi, L. Meda, A. Tacca, Chem. Soc. Rev. 42 (2013) 2228.
[18] P. Sun, Z. Deng, P. Yang, X. Yu, Y. Chen, Z. Liang, H. Meng, W. Xie, S. Tan, W. Mai, J. Mater. Chem. A 3 (2015) 12076.
[19] L. Gao, X. Wang, Z. Xie, W. Song, L. Wang, X. Wu, F. Qu, D. Chen, G. Shen, J. Mater. Chem. A 1 (2013) 7167.
[20] E. Kang, S. An, S. Yoon, J. K. Kim, J. Lee, J. Mater. Chem. 20 (2010) 7416.
[21] J. Liu, J. Jiang, M. Bosman, H. J. Fan, J. Mater. Chem. 22 (2012) 2419.
[22] P. A. Shinde, V. C. Lokhande, T. Ji, C. D. Lokhande, J. Colloid Interface Sci. 498 (2017) 202.
[23] C. Navio, S. Vallejos, T. Stoycheva, E. Llobet, X. Correig, R. Snyders, C. Blackman, P. Umek, X. Ke, G. V. Tendeloo, C. Bittencourt, Mater. Chem. Phys. 134 (2012) 809.
[24] Y. Zhao, P. Jiang, S. S. Xie, J. Power Sources 239 (2013) 393.
[25] N. Yu, H. Yin, W. Zhang, Y. Liu, Z. Tang, M. Q. Zhu, Adv. Energy Mater. 6 (2016) 1501458.
[26] J. Zhi, O. Reiser, F. Huang, ACS Appl. Mater. Interfaces 8 (2016) 8452.
[27] D. P. Dubal, G. S. Gund, R. Holze, H. S. Jadhav, C. D. Lokhande, C.-J. Park, Electrochim. Acta 103 (2013) 103.
[28] C. Yuan, H. Lin, H. Lu, E. Xing, Y. Zhang, B. Xie, Mater. Lett. 148 (2015) 167.
[29] P. A. Shinde, A. C. Lokhande, N. R. Chodankar, A. M. Patil, J. H. Kim, C. D. Lokhande, Electrochim. Acta 224 (2017) 397.
[30] P. Barbara, Z. Daniel, B. Sergio, J. Phys. Chem. C 118 (2014) 4103.
[31] L. Gao, F. Qu, X. Wu, J. Mater. Chem. A 2 (2014) 7367.